



4D imaging of polymer electrolyte membrane fuel cell catalyst layers by soft X-ray spectro-tomography

Juan Wu^a, Lis G.A. Melo^a, Xiaohui Zhu^a, Marcia M. West^b, Viatcheslav Berejnov^c, Darija Susac^c, Juergen Stumper^c, Adam P. Hitchcock^{a,*}

^a Dept. of Chemistry & Chemical Biology, McMaster University, Hamilton, L8S 4M1, Canada

^b Dept. of Pathology, McMaster University Hamilton, L8N 3Z5, Canada

^c Automotive Fuel Cell Cooperation (AFCC) Corp., Burnaby, V5J 5J8, Canada

HIGHLIGHTS

- Soft X-ray tomography at multiple X-ray energies is used to map ionomer in PEM-FC.
- Compressed sensing processing allows valid reconstruction with ~15 tilt angles.
- Multi-set tomograms are used to guide dose reduction to get low damage measurements.
- Changes in 3D ionomer distribution occur due to radiation damage.
- Conditions to achieve low damage (< 5%) are identified and used for 4D imaging.

ARTICLE INFO

Keywords:

X-ray microscopy
Tomography
3D ionomer distributions
STXM
Compressed sensing
Radiation damage

ABSTRACT

4D imaging - the three-dimensional distributions of chemical species determined using multi-energy X-ray tomography - of cathode catalyst layers of polymer electrolyte membrane fuel cells (PEM-FC) has been measured by scanning transmission x-ray microscopy (STXM) spectro-tomography at the C 1s and F 1s edges. In order to monitor the effects of radiation damage on the composition and 3D structure of the perfluorosulfonic acid (PFSA) ionomer, the same volume was measured 3 times sequentially, with spectral characterization of that same volume at several time points during the measurements. The changes in the average F 1s spectrum of the ionomer in the cathode as the measurements progressed gave insights into the degree of chemical modification, fluorine mass loss, and changes in the 3D distributions of ionomer that accompanied the spectro-tomographic measurement. The PFSA ionomer-in-cathode is modified both chemically and physically by radiation damage. The 3D volume decreases anisotropically. By reducing the incident flux, partial defocusing (50 nm spot size), limiting the number of tilt angles to 14, and using compressed sensing reconstruction, we show it is possible to reproducibly measure the 3D structure of ionomer in PEM-FC cathodes at ambient temperature while causing minimal radiation damage.

1. Introduction

Quantitative imaging of the chemical components of polymer electrolyte membrane fuel cell (PEM FC) electrodes is needed to analyze catalyst layer (CL) fabrication quality and failure modes [1]. The 3D distribution of the components in CLs determines porosity and thus permeability for fuels and products; electrochemical effectiveness, and thermo-mechanical properties. Analytical electron microscopy and X-ray microscopy both have the spatial resolution and chemical sensitivity to provide useful analytical information about CL components.

However, the electron and X-ray beams cause radiation damage [2–4] in soft materials such as biological materials [5] and polymers [4,6,7] and is a major limitation in analytical microscopes which use ionizing radiation. Radiation damage brings into question the reliability of the quantitation, especially for the perfluorosulfonic acid (PFSA) ionomer component which is extremely radiation sensitive [8–10]. The electron beam in Transmission Electron Microscopy (TEM) and the photon beam in X-ray microscopy (XRM) both inject energy into the sample and cause radiation damage, the severity of which depends on the sample and method used [2,3]. Changes to the chemical composition, structure

* Corresponding author.

E-mail address: aph@mcmaster.ca (A.P. Hitchcock).

and spatial distributions caused by radiation damage can limit effective spatial resolution and definitely limit analytical accuracy. In order to obtain meaningful analytical results, it is important to understand how the analytical spectral signal changes both qualitatively and quantitatively, and to characterize the physical and chemical changes that occur.

This study focuses on the PEMFC cathode catalyst layer, which is composed of graphitic carbon support particles decorated with Pt catalyst, and the ionomer proton conductor, perfluorosulfonic acid (PFSA). The spatial distribution of catalyst particles and ionomer in a PEM-FC cathode affects the efficiency of the fuel cell device since the oxygen reduction reaction (ORR) at the cathode is the rate limiting process. For the ORR to occur, protons must be transported along a continuous pathway of PFSA from the membrane/cathode boundary to all of the ORR catalyst sites throughout the cathode. Since the reaction only happens at the interface of PFSA, catalyst particles, conductive carbon support, and with access via a porous network to O₂ reactant and product water removal, it is important to accurately measure the distribution of PFSA and pores, not only in 2D [11–16], but also in 3D [17–20].

Hard X-ray tomography in the laboratory [21,22] and at synchrotrons [23] is well-developed, and has been used for 3D characterization of the gas diffusion layer (GDL) [24] as well as tracking liquid water transport in model PEM-FC structures [25,26]. The microstructure of the solid phase of PEMFC electrodes [22] and changes in PEM-FC membranes following transient operation [26] have also been studied by X-ray computed tomography. However, the lab and most synchrotron hard X-ray methods do not provide chemical analysis and have a spatial resolution of ~1 μm at best. Saida et al. [27] have used full field X-ray microscopy, and spectro-laminography at the Pt L₃ edge, to characterize the oxidation state of the Pt catalyst in fresh and degraded PEM-FC MEAs, with a spatial resolution of 1.5 μm (x,y) and 5 μm (z). Very recently, Matsui et al. [28] have reported *operando* spectro-tomography at the Pt L₃ edge, thereby providing 3D chemical maps of Pt in the catalyst layer before and after *in situ* accelerated degradation testing (total of 20,000 cycles). Again the spatial resolution was a few μm. In both cases [27,28] complete Pt L₃ spectra were acquired. These are outstanding measurements which provide important chemical state information on the Pt catalyst but little or no information on the morphology and chemical state of the low-Z support, ionomer and membrane components of the membrane.

Soft X-ray tomography has higher spatial resolution (~30 nm [29]) than hard X-ray tomography and excellent analytical capability if tomograms at multiple photon energies are measured. 3D density based imaging using full field transmission soft X-ray microscopes is well developed [30]. However it has not been applied to PEM-FC to our knowledge, and does not provide spectroscopy in most implementations. Soft X-ray STXM tomography using multiple photon energies for direct 3D chemical mapping, was pioneered by Johansson et al. [31–35]. A comprehensive review of soft X-ray STXM spectro-tomography, which includes results on PEM-FC and related materials, was published recently [36].

Soft X-ray STXM [37–40] has been demonstrated to be a useful method for quantitative chemically sensitive imaging of the PEM-FC

cathode catalyst layer, and in particular, for giving accurate 2D projection maps of the ionomer in PEM-FC cathodes with negligible radiation damage [10–16,40]. Over the last few years, our group has been working to extend STXM characterization of cathode catalyst layers to 4D imaging which involves multi-photon energy tomography, or imaging in four dimensions (x, y, z, E). 4D imaging measures the spatial distribution of each chemical species of a heterogeneous sample in 3D. Prior to this study, STXM tilt-series spectro-tomography at the C 1s and F 1s edges was applied to two types of pristine catalyst coated membranes (CCM), demonstrating that the ionomer in the cathode could be visualized in 3D [19]. However, the 3D spatial resolution was somewhat less than the 2D spatial resolution, and the morphology and ionomer amount was significantly modified by the large radiation doses used in those studies [19]. The doses used in that early work were large – many 100's of MGy - because the same volume was measured repeatedly at multiple photon energies and multiple tilt angles, using maximum usable incident flux.

The objective of the research reported in this paper is to find ways of performing room temperature STXM spectro-tomography with significantly reduced dose so as to perform 4D imaging of the PFSA ionomer in a real PEM-FC cathode sample without extensive fluorine mass loss, without modification to the ionomer distribution, and without changes to the local chemical structure of the PFSA. To guide the operational changes that have allowed us to achieve this goal, we have developed a multi-set tomography method which tracks the mass loss, chemical transformation, and 3D structural reorganization of PFSA in PEM-FC cathodes during tomography. A major improvement was the use of a new reconstruction method called compressed sensing [41]. By combining compressed sensing tomographic reconstruction, reducing the number of tilt angles, and a 50-fold reduction in incident flux, we show that it is possible to measure meaningful, quantitative 3D ionomer-in-cathode distributions of real PEM-FC samples using STXM spectro-tomography at ambient temperature.

2. Materials and methods

2.1. Samples

Several different fuel cell PEM-FC catalyst coated membrane (CCM) samples were used in this study. Table 1 summarizes their compositions and properties. The CCMs were cut into small rectangular pieces and embedded in an amine epoxy resin (called TTE for short), prepared by mixing trimethylolpropane triglycidyl ether and 4,4'-methylenebis(2-methylcyclohexylamine) in a 1:1 wt ratio and cured at 70 °C overnight [42]. The embedded samples were microtomed at room temperature using a DiATOM[™] diamond knife with a Leica Ultracut UCT to generate sections with nominal thicknesses between 100 and 300 nm. The sections were transferred from the surface of a water bath to formvar coated 100-mesh Cu TEM grids, which were then used for STXM studies.

There are size constraints in the STXM chamber which are important for tomography measurements [36]. The distance from the sample to the order sorting aperture (OSA), which is the first optical element upstream from the sample, is only 250 μm when measuring at

Table 1
Properties of the MEA samples examined in this work.

Sample label	source	Membrane	C_support	Ionomer	I/C ^a	Pt load (mg/cm ²) ^a	Cathode fabrication method
MEA "C" 2071 TMP	Gore	ePTFE micro-reinforced; Gore-Select, 18 μm	Gore LSAC	Gore		0.4	Slot-die coating
MEA "A"	AFCC	Continuous; NRE-211, 25 μm, 1100EW	LSAC	Nafion 117	1.44	0.25	Mayer bar coating
MEA "B"	AFCC	Continuous; NRE-211, 25 μm, 1100EW	LSAC	Nafion 115	0.57	0.25	Mayer bar coating
MEA 11 GDE	Ballard	Continuous; NRE-211, 25 μm, 1100EW	LSAC	Nafion 117	1.07	0.6–0.7	Screen print

^a Target values, defined from ink composition.

Table 2
Summary of conditions for experimental measurements.^a

Code	sample	STXM	Type	Fig(s)	Energies (eV)	Angles (°)/#	Io (MHz) ^b	Beam diam (nm)	Step size (nm)	Thickness (nm) ^c	Total dose (MGy) ^{c,d}
A1	MEA-C in PS	ALS 5.3.2.2	2D C 1s	1	C 1s: 278–324/86	0	15.6 ^e	120	120	110	9
A2	MEA-C in PS	ALS 5.3.2.2	2D F 1s	1	F 1s: 680–740/70	0	4 ^f	150	150	110	4
B1	MEA-C in PS	ALS 5.3.2.2	3D lo-dose 1-set	S-3	C 1s: 278.0, 284.5, 285.3	–72 to +64/35 total	7.7	80	80	110	8
B2	MEA-C in PS	ALS 5.3.2.2	3D lo-dose 1-set	S-3	F 1s: 684, 694	–72 to +64/35 total	3.4	80	80	110	13
C	MEA-A in TTE	ALS 5.3.2.2	3D hi dose 3-set (3°) ^g	S-3	F 1s: 684, 694	–66 to +60 /15 per set	9.4	45	45	310	72
D	MEA-A in TTE	ALS 1102	3D hi dose 3-set (3°) ^g	S-4, S-5, S-6	F 1s: 684, 694	–66 to +60 /15 per set	20 ^h	30	30	61	780
E1	MEA-A in TTE	ALS 1102	3D mid dose 2-set (6°) ^{g,i}	S-6, S-7	C 1s: 278, 285.4	–60 to +60 /16 per set	20.6 ^h	40	40	95	52
E1	MEA-A in TTE	ALS 1102	3D mid dose 2-set (6°) ^{g,i}	S-6, S-7	F 1s: 684, 694	–60 to +60 /16 per set	4 ^h	40	40	95	8
E2	MEA-A in TTE	CLS aSTXM	3D lo dose 2-set (6°) ^g	S-6, S-7	C 1s: 278, 285.4	–60 to +60 /16 per set	1.9	50	50	95	4
E2	MEA-A in TTE	CLS aSTXM	3D lo dose 2-set (6°) ^g	S-6, S-7	F 1s: 684, 694	–60 to +60 /16 per set	3.3	50	50	95	6
F1	MEA-A in PS	ALS 5.3.2.2	3D lo dose 3-set (3°) ^g	4–6	F 1s: 684, 705	–66 to +60 /16 per set	4.1	50	50	177	32
F2	MEA-A in PS	ALS 5.3.2.2	3D 1-set	4–6	C 1s: 280, 284.5	–66 to +60/15	5	50	50	177	6
G	MEA-11 GDE	CLS aSTXM	3D lo dose 3-set (3°) ^g	7,8	F 1s: 684, 705	–63 to +54 /14 per set	2.3	50	50	336	10

^a For each image the dwell time per pixel is 1 ms. The voxel size used in the reconstruction is the same as the step size of the images.

^b The Io signal is the measured value divided by the detector efficiency which is different for the different beamlines used. For ALS 5.3.2.2 and CLS a-STXM measured detector efficiencies of 0.7 (F 1s) and 0.3 (C 1s) were used. For 11.0.2 detector efficiencies of 0.4 (F 1s) and 0.15 (C 1s) were used.

^c Thickness and dose estimated for the membrane region.

^d For A, B, E, and F the total dose (sum of C 1s and F 1s) are 13, 21, 70 and 38 MGy.

^e At 319 eV.

^f At 705 eV.

^g Angle increment between individual sets of the multi-set acquisition.

^h For the data collected at 1102, the Io indicated was not normalized by the detector efficiency.

ⁱ Both C 1s and F 1s tomography data was measured for code E at ALS 11.0.2 but it was of poor quality so it was re-measured at CLS. The E1 dose combines dose from both the F 1s and C1s measurements at ALS 11.0.2.

the C 1s edge [37]. To allow for sample rotation without collisions between the sample and the OSA at high tilt angles, it is necessary to reduce the lateral width of the sample. Thus, the TEM grid was cut using a fresh scalpel to isolate a single, ~250 μm wide strip containing the CCM section of interest. This grid strip was then glued at the tip of a metal pin, which was held in a mechanical pencil chuck, which in turn was secured to the shaft of a stepping motor rotator.

2.2. Instrumentation and methods

STXM measurements were performed at room temperature using the ambient STXM at Canadian Light Source (CLS) beamline 10ID-1 [43] and STXMs on Advanced Light Source (ALS) beamlines 5.3.2.2 [44] and 11.0.2 [45]. The details of STXM instrumentation and principles of operation are described elsewhere [37–39,46]. Image contrast and thus chemical sensitivity in STXM is based on the near-edge X-ray absorption fine structure (NEXAFS) [47] spectral response of the different materials in heterogeneous samples such as PEM-FC cathodes. NEXAFS spectral signals measured in transmission under conditions where the Beer-Lambert law applies provide a high degree of chemical sensitivity and can be used to quantify the amounts of each species at each pixel or voxel (expressed as nm thickness). STXM measurements using 2D projection have been used widely in PEMFC cathode catalyst research [10–16,41]. In this work, the spectro-tomography measurements were performed using only a few specific energies at the C 1s and F 1s absorption edges since these suffice to map spatial distributions of carbon support, PFSA ionomer, Pt catalyst and porosity [10–15].

STXM tomography is performed by mounting the sample on a rotation system, with the rotation axis perpendicular to the propagation direction of the incident X-ray beam. The STXM angle-scan tomography rotation stage (Supplemental Fig. S-1a) uses a two-phase micro-stepper motor (Faulhaber ADM0620, Faulhaber, Schoenaich, Germany). The strip cut from the TEM grid containing the MEA sample is mounted on a 0.8 mm diameter brass pin, inserted in a chuck from a mechanical pencil, which in turn, is mounted on the motor shaft (see Fig.S-1b). The position and orientation of the sample strip is carefully adjusted under an optical microscope to align the sample region of interest with the rotation axis, which is perpendicular to the incident X-ray beam. With care, the extent of off-axis motion during 180° rotation can be reduced to ~50 μm [35].

Due to attenuation of the soft X-ray beam at high angles for flat samples the maximum rotation angle that can be measured is ~80°; usually the angle range is limited to ± 70°. Note that with focused ion beam (FIB) pillar or cylindrical samples such as pulled glass pipettes [33] it is possible to rotate over the full 180° range. The range and angle increments for each measurement made in this work are summarized in Table 2. After each rotation, the region of interest had to be located and the microscope refocused. This increases the operation time and results in some additional dose. Good alignment of the spatial orientation of the grid sample strip along the rotation axis decreases this extra operational time since the region of interest stays close to the X-ray beam at all tilt angles. At present, among soft X-ray STXMs, only the Nano-surveyor I system at ALS [48] is equipped with a proper eucentric sample adjustment system, which is needed to fully automate STXM

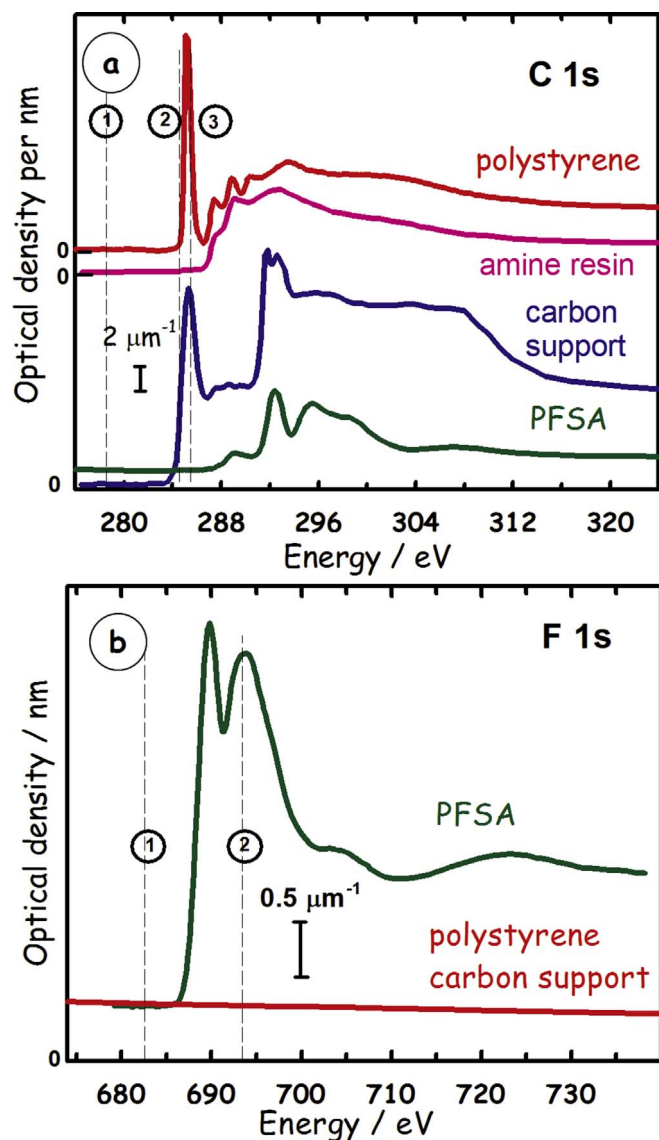


Fig. 1. (a) C 1s spectrum of perfluorosulfonic acid (PFSA), the membrane of a catalyst coated membrane (CCM) of a polymer electrolyte membrane fuel cell (PEM-FC), recorded with scanning transmission X-ray microscopy (STXM) using a defocused beam, with conditions in code A (Table 2). The C 1s spectra of the carbon support and the amine epoxy (TTE) and polystyrene (PS) embedding materials used in these studies are also plotted. The intensity scale is absolute (OD/nm) and offsets are used for clarity. (b) F 1s spectrum of PFSA and the spectral response of carbon in the F 1s region. (measured at ALS 5.3.2.2).

tomography data acquisition. Despite this lacuna of the STXMs used in this work, the trajectory of the rotation can be predicted if one measures several images at large angle changes (e.g. -45° , 0° , $+45^\circ$) and does some simple trigonometry. This approach can save significant measurement time. In the past, most soft X-ray STXM tomography acquired images at 30–40 tilt angles [31–36]. Tomography measurements of a PEM-FC MEA sample at two absorption edges (4 photon energies), 39 tilt angles, $10 \mu\text{m} \times 10 \mu\text{m}$ image size with 200×200 pixels takes 10–12 h, despite the actual image data acquisition time being only 3–4 h. However, with the development of compressed sensing 3D reconstruction methods [49,50], good quality reconstructions can be achieved with 10 or even fewer tilt angles [39] which significantly reduces both the beamtime used and the imparted dose. Different experimental conditions and different STXM microscopes and beamlines were used for the various tomography data sets reported in this paper. The parameters for each data set are summarized in Table 2, using code

X as the label for each measurement.

2.3. Spectroscopy and STXM data analysis

Axis2000 [51] is used to convert the measured transmission intensity images to optical density (OD) images by applying the Lambert-Beer law at each image pixel:

$$OD(E) = \ln(I_0(E)/I(E)) = \sum_i \mu_i(E)\rho_i t_i \quad (1)$$

where $I_0(E)$ is the intensity spectrum of the incident X-ray, $I(E)$ is the intensity spectrum of the transmitted beam, $\mu_i(E)$ is the X-ray absorption coefficient, ρ_i is the density and t_i is the thickness of component i . If suitable reference spectra are available, and they have been placed on an absolute intensity scale (OD/nm, also called OD1), then the absolute thicknesses of each component at each pixel can be derived, assuming the local density is the same as that of the pure material [39].

The procedure used to derive quantitative component maps at each tilt angle is the same as that used for 2D projection mapping [11–13] – two energies at the C 1s are used to map carbon support, 2 energies at the F 1s are used to map ionomer, and the F 1s data is combined with the pre-C 1s image to map the Pt catalyst [13]. In a few cases (codes, C, D, G) the non-fluorinated 3D distributions of non-fluorinated components were derived from the pre-F 1s edge tomogram, by subtracting a weighted amount of the ionomer tomogram signal, to correct for the absorption by ionomer at the pre-edge energy. Before each tomography measurement, images at a series of photon energies (called a stack [52]) in the C 1s and F 1s regions are acquired and analyzed to determine the optimum energies for the 2-energy (on/off) evaluation. Fig. 1 presents quantitative C 1s and F 1s spectra of the chemical species involved. The calibration and pre-tomography characterization is performed using a full spectral stack (50–70 images), which is measured in a different region to the tomography area, but one with similar morphology. In order to map the PFSA and the carbon support with minimal radiation dose, images are measured at only 4 energies. The on-signal for carbon support is measured at 284.5 eV for polystyrene (PS) embedded samples and 285.2 eV for TTE embedded samples. The on-signal for PFSA ionomer is measured at 694 eV or 705 eV. Initially we used 694 eV, since this peak has high intensity and was very sensitive to radiation damage. However during the course of this study we realized the changes at 694 eV were a combination of electronic/chemical structure changes and fluorine loss, which have similar decay rates at low dose, but diverge at higher doses. Since it was more important to track the amount of fluorine with respect to quantitation, we changed our on-signal energy to 705 eV. At energies in the F 1s continuum such as 705 eV, the F-loss is accurately measured without combining sensitivity to electronic/chemical structure changes. The off-signal is measured at a pre-edge energy where absorption by all components is tracked (278 eV for carbon support, and 684 eV for PFSA). After converting each image to optical density (OD), chemical maps of each component are generated by subtracting the pre-edge image from the absorption peak image (e.g. for a TTE-embedded sample, $OD_{\text{Csup}} = OD_{285.2} - OD_{278}$, and $OD_{\text{PFSA}} = OD_{694} - OD_{684}$).

The methods used to derive doses for each experiment are detailed in Supplemental Information, section S-1.

2.4. Tomography data acquisition and analysis

A flow diagram of the tomography data acquisition and analysis is shown in Fig. 2. Data with various choices of tilt angles were measured in this work in order to systematically find ways to reduce dose while preserving 4D imaging quality. Table 2 summarizes details of each measurement. At each angle, images measured at either or both the C 1s and F 1s edges are converted to quantitative maps of the carbon support and ionomer. The individual images or the chemical maps at a set of projection angles are then aligned in aXis2000 using Fourier correlation

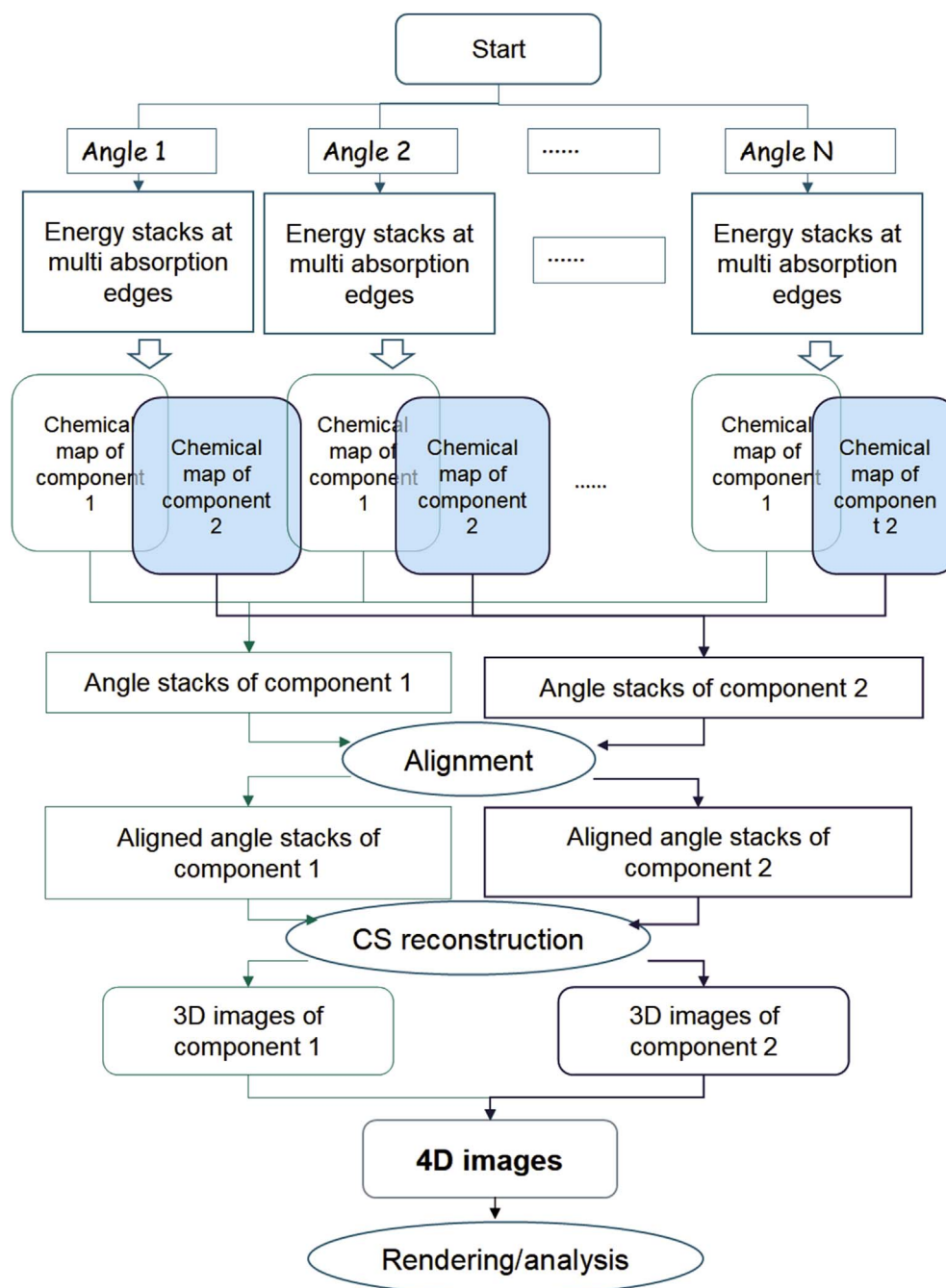


Fig. 2. Flow diagram of STXM tomography data acquisition and processing.

methods. A final alignment based on sinusoidal response optimization is performed using IMod [53] or TomoJ [54]. The fully aligned tilt angle data sets (single energy images or chemical maps) are used for 3D reconstruction by IMod, TomoJ or Mantis [41,55,56]. Different reconstruction algorithms can be employed. One of the most popular 3D reconstruction algorithms is SIRT (Simultaneous Iterative Reconstruction Technique) [57]. However, SIRT requires data from at least 30 tilt angles over a wide-angle range to obtain good quality reconstruction. For STXM tomography, measuring this many tilt angles results in long exposure times and excessive radiation damage to the ionomer. In this study, the 3D reconstructions were performed using a compressed sensing algorithm [58] developed by Lerotic [41] which is available in the Mantis package for spectromicroscopy analysis [56]. The compressed sensing (CS) approach provides high quality 3D reconstructions on data sets with a significantly reduced number of projection angles

[41]. CS is also less sensitive than SIRT to missing wedge artifacts associated with limited tilt angle ranges. By using CS, the tomography measurement time can be significantly decreased because 10 tilt angles over $\pm 70^\circ$ provides a reconstruction quality which is as good or better than SIRT analysis of a 40 tilt angle data set [41]. The compressed sensing algorithm parameters were tested and adjusted for different data sets. For the PEM-FC cathode samples, a β parameter of 0.1, and 30 iterations were typically used. There is another important advantage to use the CS method. Since good quality reconstruction can be obtained using only 10 images [41], we were able to make several tomographic measurements on the same area with gradually increasing dose. This enabled exploration of the effects of radiation damage on the quantitative 3D ionomer distribution and the chemical state of the ionomer.

By merging the reconstructed 3D data sets of the ionomer and carbon support, a 4D image (chemically sensitive 3D imaging) is

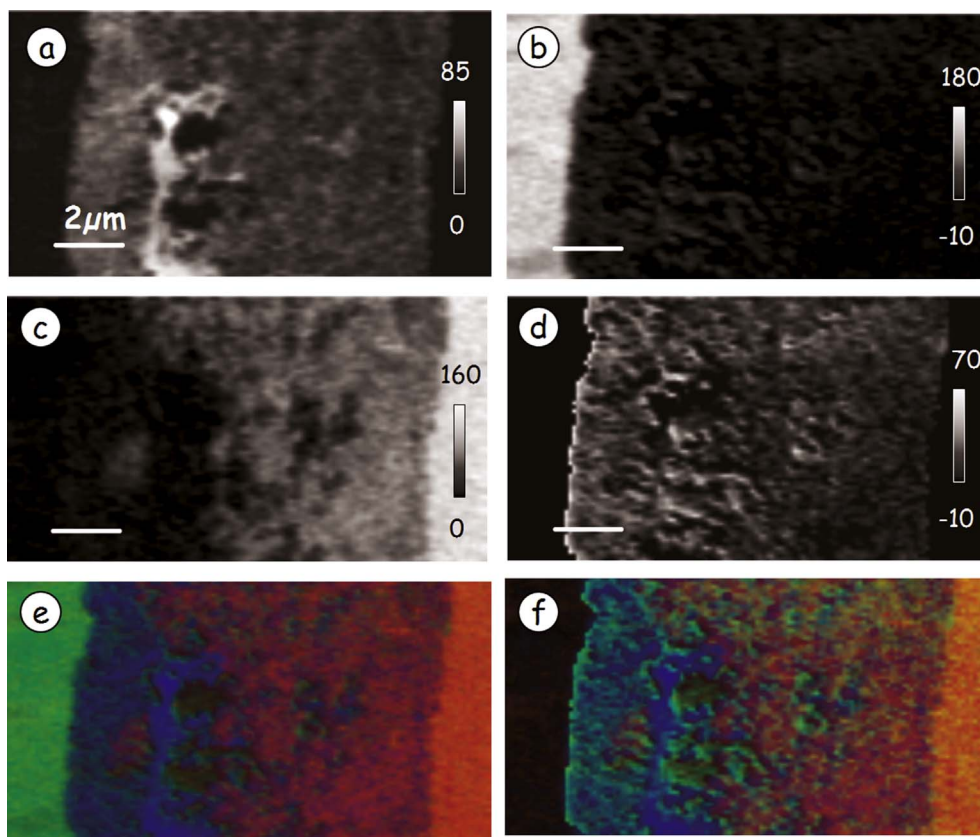


Fig. 3. Component maps of (a) carbon support, (b) PFSA, (c) polystyrene, (d) ionomer in cathode, derived from a stack fit of OD1 reference spectra (Fig. 1), and a constant fit to a C 1s stack (89 images from 278 to 324 eV), code A (see Table 2 for conditions). The intensity gray scale is thickness in nm. The ionomer map was obtained by masking and subtracting the much more intense membrane signal in the PFSA map. (e) Color coded composite using rescale (ie relative distribution) of carbon support (blue), all PFSA (green) and polystyrene (red). (f) Color coded composite of carbon support (blue), ionomer (green) and polystyrene (red) in the cathode. (measured at ALS 5.3.2.2).

generated which consists of the 3D distribution of each component within the same sample volume with accurate spatial registry. Alternatively, it is possible to perform the analysis of all the spectral and angle data in Mantis, such that the spectral data at any set of voxels in the reconstructed volume can be extracted, examined and analyzed [41]. All reconstructions were performed using cubic voxels with a side dimension equal to the step (pixel) size in the 2D images (see Table 2 for details). Segmentation, visualization and rendered displays, both stills and movies, were performed using Chimera [59], TomoJ [54] or Avizo 9.0 [60]. For isolating 3D distributions of specific components the automated Otsu threshold method [61] was used to guide segmentation. The explicit thresholds used for each rendering are listed in the figure captions.

3. Results

3.1. Spectroscopic analysis and tomography of PEM-FC cathodes

Typical C 1s and F 1s X-ray absorption spectra of the chemical components of PEM-FC cathodes, as well as TTE and PS, the two embedding media used in this work, are presented in Fig. 1a. All but the TTE spectrum were measured on sample MEA “C” embedded in PS, using conditions in code A, which deposited approximately 9 and 4 MGy for the C 1s and F 1s measurement, respectively, and thus negligible damage is expected. The carbon support (typically partially graphitic carbon black), the PFSA, and the embedding media (either polystyrene or amine resin) can be easily differentiated from their C 1s spectra (Fig. 1a). In addition, it is possible to estimate the amount of Pt catalyst present from the pre-C 1s intensity combined with knowledge of the amount of PFSA, as explained and used in a recent study [13]. For the F 1s edge, PFSA is the only F-containing component; the other carbon-rich components have a similar, non-structured shape in the F 1s region (Fig. 1b). Thus, it is straightforward to quantitatively map ionomer-in-cathode from the F 1s spectrum using the 2-energy stack

map procedure [10–12]. As an example of STXM 2D chemical mapping, Fig. 3 presents quantitative component maps of the carbon support, PFSA and the polystyrene (PS) embedding media, derived from a C 1s stack recorded from MEA “C” at 86 energies from 278 to 324 eV. Color composites of these component maps are presented in Fig. 3e (PS – red, membrane & ionomer – green, carbon – blue, over the whole region measured) and Fig. 3f (PS – red, ionomer-in-cathode – green, and carbon – blue). Such color composite maps are very useful to display the relative spatial positions of the components, which is obviously critical to understanding the relationship of processing, distributions of PFSA ionomer in the cathode, and PEM-FC performance. The radiation dose caused by the combined F 1s and C 1s stack measurements is estimated to be 13 MGy, which is about 1/3rd of the PFSA thin film critical dose (Table 2, code A). Tomography measurements were also performed as per code B. The tomographic results, damage evaluation and associated discussion are presented in Supplemental Information section S-2, which includes visualization (Fig. S-2).

3.2. Three-set F 1s spectro-tomography of a thick sample with high dose (code C)

A three-set F 1s spectro-tomography study was carried out on a ~300 nm thick MEA “A” sample (measurement as described in code C in Table 2), using a radiation dose rate of 750 MGy/s and a total dose of 72 MGy. This is a high dose rate, but is typical of the values used for 2D projection mapping of ionomer in cathode, since high statistical precision can be obtained with less than 5 ms total dwell per pixel [11,12]. Each of the three tilt-angle tomography data sets consisted of measurements at 15 angles. Set 1 was measured from -66° to $+60^\circ$ with 9° increment, while the angles for set 2 were offset by $+3^\circ$, and those for set 3 were offset by $+6^\circ$, thereby covering the full range of -66° to $+66^\circ$ for a total of 45 angles. The F 1s spectrum of the cathode was measured using a defocused beam before and after each tomography data collection, using only 3.4 MGy dose per stack. Fig. 4a shows there

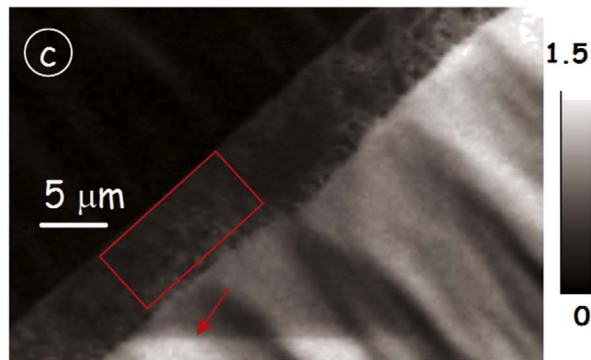
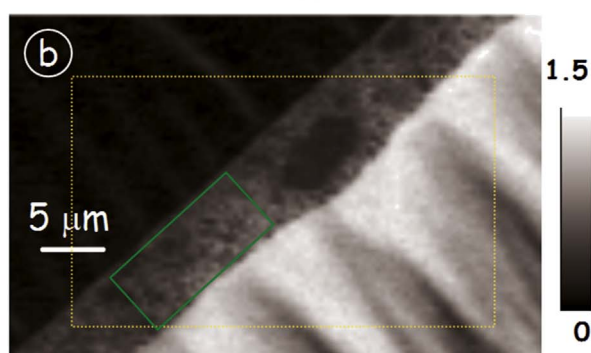
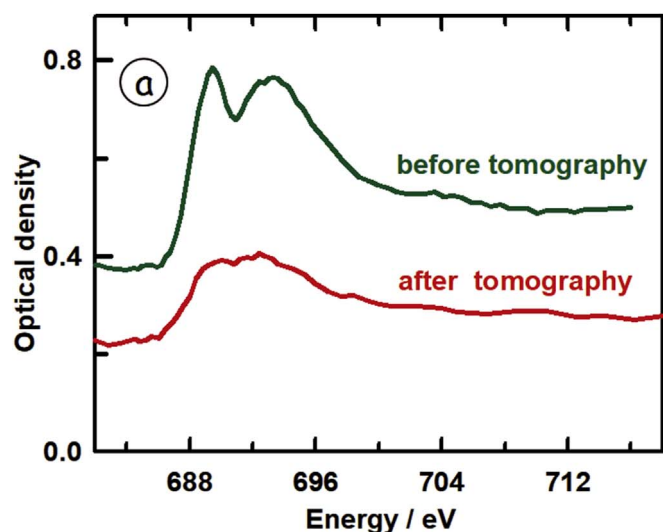


Fig. 4. Average F 1s spectra of PFSA in cathode of MEA-A, tomography measurement **code C** (Table 2), before and after 3 set spectro-tomography. Optical density image at 694 eV, (b) before, and (c) after 3-set tomography. The rectangular frame in (b) indicates the tomography region, which is evident in (c) from contrast changes at the boundary in the cathode and membrane areas due to radiation damage. The areas from which the cathode F 1s spectra were obtained are also indicated. (measured at ALS 5322).

was a significant reduction in the intensity of the F 1s spectrum of the PFSA cathode after the tomography dataset acquisition, which imparted a total dose of 72 MGy. After the full 3 set tomography measurement, there is only a hint of the two peak spectrum typical for undamaged PFSA, and the F 1s continuum signal has decreased by $\sim 50\%$ relative to the adjacent undamaged area. This extent of fluorine loss would invalidate these results as a quantitative evaluation of the distribution of ionomer in cathodes. The radiation damage causes a significant change in contrast as visualized by comparing an OD image measured at 694 eV before (Fig. 4b) and after (Fig. 4c) the 3-set tomography measurements.

Since three independent tomography measurements were made on the same volume it is possible to test for spatial selectivity in the fluorine loss. Fig. 5a,b,c display the 2D fluorine maps at \sim normal

incidence (-3° , 0° , and 3° in the 1st, 2nd and 3rd set, respectively). The average F 1s signal ($OD_{694} - OD_{684}$) decreased by $\sim 20\%$ by the end of the first set, by another $\sim 20\%$ after the second set, and another 10% after the third set. After reconstruction, the Otsu threshold method [61] was used to segment the PFSA distributions in the cathode. Fig. 5d,e,f are 0° projections of the reconstructed ionomer signal. A significant reduction in amount of fluorine signal is evident. Fig. 5g illustrates the change (ionomer lost) in measuring set 1, displayed in red, evaluated from the difference of set 1 and set 2, superimposed on the distribution of set 2. Fig. 5h plots the same for the F loss in both sets 1 and 2, superimposed on the distribution of set 3. Clearly there is spatial selectivity in the ionomer loss, with some areas losing fluorine faster than other areas, as indicated by the non-uniform distribution of the ionomer lost. In general, the greater percent loss occurred in regions with relatively low amounts of ionomer. If the volume of ionomer after set 1 is defined as 100%, the volume of the ionomer decreased to 70% after set 2, and 50% after set 3. The total dose was 72 MGy (24 MGy for each set). The radiation effects and quantitative dose issues are discussed in section 4.

3.3. Results from multi-set spectro-tomography of other samples at high doses (codes D, E)

Supplemental Information section S-3, which includes supplemental Figs. S-3 and S-4, presents results from a three set F 1s spectro-tomography of a thin sample with high dose (**code D**). Supplemental Information section S-4, which includes supplemental Figs. S-5 and S-6, presents results from a two-set C 1s and F 1s spectro-tomography at medium dose (**code E**).

3.4. Three-set F 1s spectro-tomography with low dose F (code F)

An additional low dose 3-set tomography measurement was performed on a 200 nm thick section of sample MEA-A, with conditions of **code F** (Table 2). To further reduce radiation damage while measuring the ionomer at the F 1s edge, the F 1s tomography data was measured first, then the C 1s tomography data was measured, instead of taking 2 F 1s, and 2 C 1s images at each tilt angle. With this approach, the absorbed dose during the F 1s measurement was lower and thus the critical ionomer distribution less affected. The beam spot size was also defocused to 50 nm. The peak energy of the F 1s measurement was changed to 705 eV (in the F 1s continuum) in order to desensitize the 3D distributions to the change in spectral shape from 2-peak to 1-peak that occurs because of radiation damage [62]. Table 3 lists the estimated radiation dose after each step in the 3 set F 1s measurement. The total dose for all 3 F 1s tomograms was only 32 MGy.

The F 1s spectra of the cathode at different times throughout the F 1s 3-set tomography are plotted in Fig. 6. These F 1s spectra were recorded using highly defocused stacks before the tomography, after half of the first tomography set, and after each of the 3 tomography sets. By reducing the total dose to less than 32 MGy, conditions were achieved where the original 2-peak structure of the F 1s spectrum is retained throughout the whole measurement, with relatively little reduction in the F 1s continuum intensity caused by fluorine mass loss. Fig. 7 presents visualizations of the ionomer (Fig. 7a) and carbon support (Fig. 7b) components in the same volume, derived from the CS reconstruction, as well as the 4D image (Fig. 7c) combining the ionomer and carbon support reconstructions. The PFSA signal (green) was derived from $OD_{705} - OD_{684}$ while the carbon support signal (blue) was derived from $OD_{284.5} - OD_{280}$. Fig. 7d,e,f shows views from a 30° viewing angle of the 3D distributions of the ionomer (green) and carbon support (blue) components derived from each of the 3-set tomographic measurements of the same region of the cathode. Because the C 1s measurement of the carbon support was done after the F 1s measurement, there is additional uncertainty in the quantitation. Fig. 7g,h,i presents maps of the overlap (intersection) of the carbon support and

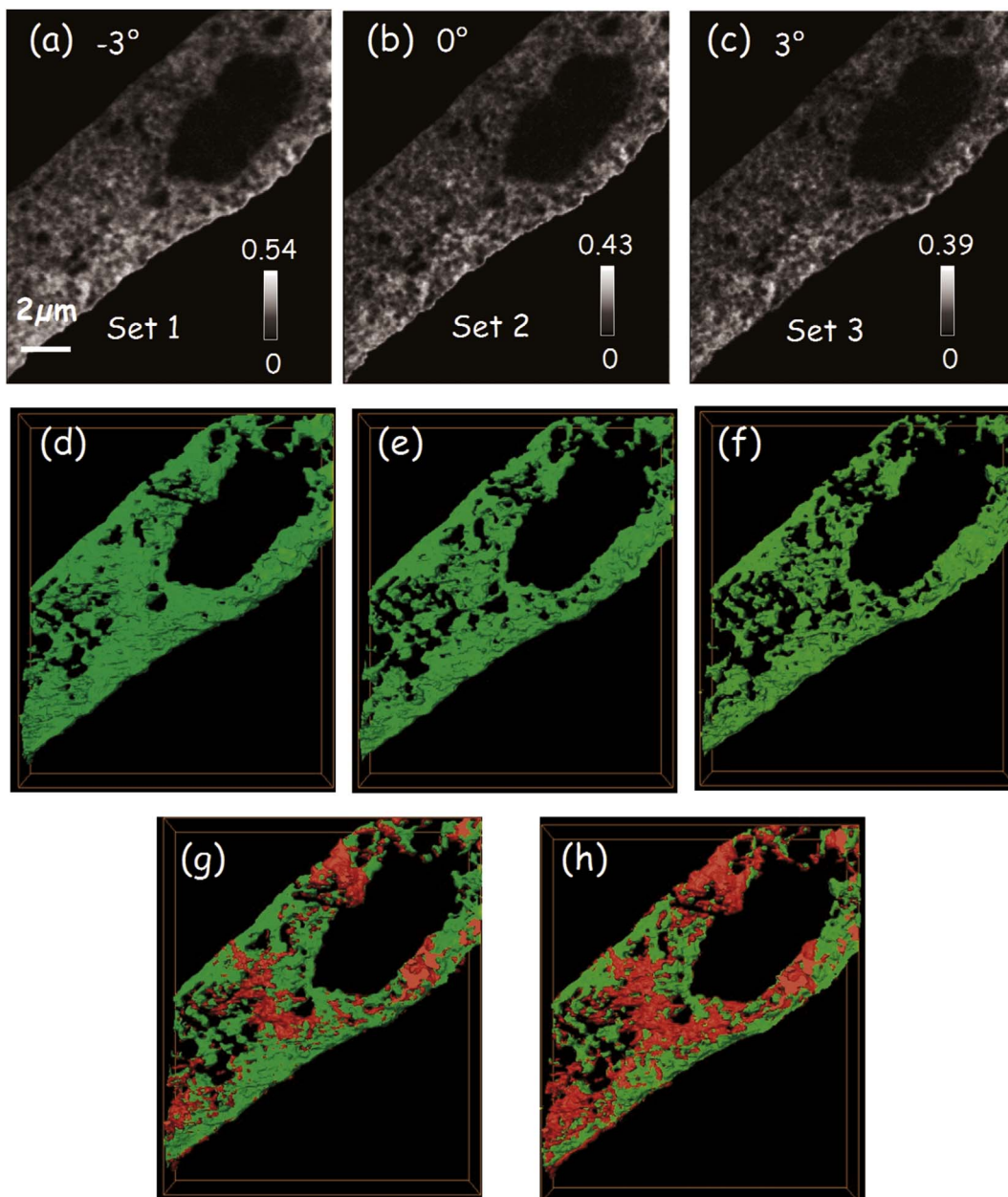


Fig. 5. 2D fluorine maps of MEA-A, tomography measurement **code C**, from F 1s stack maps measured at: (a) -3° in set 1, (b) 0° in set 2, (c) 3° in set 3 (3° offsets of the projection angle scales were used between each set). Surface renderings (indicating location) of the 3D ionomer distribution from CS reconstruction of (d) set 1, (e) set 2, (f) set 3 at 0° . Surface renderings of ionomer loss superimposed on the ionomer distribution of set 1, for ionomer loss derived from (g) difference between set 1 and set 2 in red, and for ionomer loss derived from (h) difference between set 1 and set 3 in red. The thresholds used to segment the ionomer volumes are 0.0040, 0.0050, 0.0055 for sets 1, 2, and 3. (measured at ALS 5.3.2.2).

Table 3
Accumulated radiation dose and volume fractions in the F 1s stacks in the low dose experiment (**code F**, 200 nm sample).

Set#	Radiation dose (MGy) ^a	OD ₇₀₅ - OD ₆₈₂ ^b	Thresh. C _{supp}	Carbon Support (%) ^c	Thresh. PFSA	PFSA in cathode (%) ^c	Intersection of C _{supp} . & PFSA in 3D (%)	Porosity (%) ^d	PFSA off C _{supp} (%)
1 st	12	0.127	0.005	69	0.0070	48	41	23	8
2 nd	21	0.126	0.005	69	0.0033	43	33	27	4
3 rd	30	0.122	0.005	69	0.0036	41	27	30	1

^a Cumulative radiation dose up to and including the indicated measurement from both spectroscopy and tomography measurements.

^b Prior to any measurements OD₇₀₅ - OD₆₈₂ was 0.135.

^c The volume percent for each species is determined after threshold values indicated, which were obtained with guidance from the Otsu auto-threshold method [60].

^d Porosity was determined by requiring the sum (C_{support} + PFSA_{off_support} + porosity) to equal 100%.

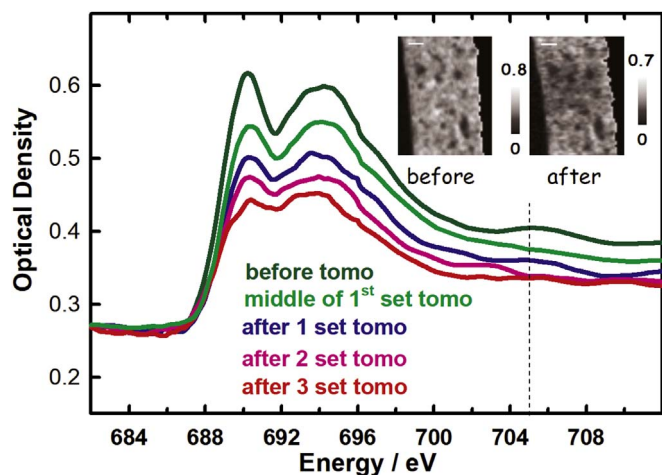


Fig. 6. F 1s spectra of PFSA in the cathode of sample MEA-A, tomography measurement code F (Table 2), taken before tomography, after 1/2 of 1st set, after 1st set, after 2nd set, and after 3rd set of the 3-set spectro-tomography. The insert images are the F maps of the tomography region before, and after the 3-set tomography measurement. (measured at ALS 5.3.2.2).

ionomer (in yellow) for sets 1,2,3, as a means for identifying the parts of the 3D distribution of ionomer that are in close proximity to the carbon support and Pt catalyst, the condition needed for effectiveness of the ionomer. The intersection volume of the carbon support and ionomer is overestimated due to the spatial resolution limitations of STXM tomography. The changes in the volume fraction of ionomer after each set are listed in Table 3. This analysis indicates that the 3D ionomer loss is more significant in regions with less ionomer and starts from areas not in contact with the carbon support. Using this approach of low flux and slightly defocused conditions, 30 tilt angles can be measured with negligible chemical change, as indicated by preservation of the 2-peaked F 1s spectrum (Fig. 6), and negligible structural change (as indicated by similarity of the 3D ionomer maps from 1st and 3rd sets), and only mild fluorine mass loss.

3.5. Three-set F 1s spectro-tomography on a thick sample with minimal dose (code G)

An additional 3-set tomography measurement was performed on a ~300 nm thick section of sample MEA 11-GDE using conditions of code G (Table 2). F 1s spectra of the cathode were recorded using large defocus, low dose conditions, before the start of tomography, at the middle of the first tomography set, then after each tomography set. The total dose after the 3-sets (total of 84 images, or 84 ms of beam at each pixel) is estimated to be 10 MGy. The F 1s spectra of the cathode recorded before, during, and after the tomography are presented in supplemental Figure S-7a. While there was a small reduction in the OD at 694 eV, the shape of the F 1s spectra remained essentially constant. The fluorine loss, as evaluated by $(OD_{705} - OD_{684})$, was only 5%. This, combined with the negligible change of spectral shape, indicates that the 3-set measurement caused negligible changes in the C-F local chemical environment or the amount of ionomer. 2D projection images at 694 eV before the start of the 3-set acquisition and after each set (supplemental Fig. S-7b through S-7e) are consistent with a very low extent of radiation damage.

Component maps of the ionomer in the cathode (obtained from $OD_{704} - OD_{684}$ at 0°) are presented in Fig. S-8(b-e). The average ionomer amount derived from these 2D maps indicates that there was only 4% fluorine mass loss by the end of the 3-set tomography, consistent with the spectral data (Fig. S-7a). Renderings of the 3D distributions of the ionomer from CS reconstruction of these tomography data sets are presented in Fig. 8. There are no significant changes between set 1 (Fig. 8a), set 2 (Fig. 8b) and set 3 (Fig. 8c) tomography results. Volume

differences in the yellow box region for set 2, as (set 2 - set 1) and for set 3 as (set 3 - set 1) are shown in Fig. 8d and Fig. 8e. The ionomer signal lost due to radiation damage is presented in red. Relative to the volume fraction of ionomer in set 1, the amount of ionomer reported in set 2 is 4.5% smaller while that reported in set 3 is 8% smaller. From the difference in total ionomer volume between the first tomography set and the second and third sets, the ionomer loss is not the same in every direction on the surface of each particle, especially during the initial stage of the radiation damage. Thus, despite relatively low radiation damage, rescaling the ionomer/voxel by the mass loss percentage will not properly represent the original 3D ionomer distribution due to selectivity in the locations where the ionomer is preferentially lost.

A movie of an Aviso rendering of the 3D distribution of the ionomer reconstructed from the code G data is presented in supplemental Section S-5. Several frames from this movie are displayed in Supplemental Fig. S-8. The voxels are cubes of 50 nm on a side. In the movie, the ionomer distribution is rotated by 360° about the tilt axis, first as measured from the first tilt angle set. It then superimposes in red the differences between set 1 and set 2 (corresponding to ionomer loss due to radiation damage in set 1), plotted on an enhanced intensity scale, relative to that of the ionomer by ~2. This clearly shows preferential loss of ionomer in the thinner regions. It then displays a 360° rotation about the tilt axis of the ionomer distribution as measured from the second tilt angle set. Finally, the differences between set 3 and set 2 ionomer results is superimposed in red, using the same, expanded intensity scale.

Supplementary video related to this article can be found at <http://dx.doi.org/10.1016/j.jpowsour.2018.01.074>.

The ionomer distributions for all three of the PEM-FC cathode samples measured in this work show large ovoidal regions where there is little or no ionomer, despite the presence of Pt coated carbon support particles in these same ovoidal regions. The origin of these ionomer-depleted regions is likely due to incomplete mixing of the ionomer with other components of the ionomer ink at the relatively large ionomer loadings that were chosen for these samples. In other studies, STXM has been used to show that lower ionomer loadings, different ink formulations, and/or different electrode layer fabrication methods can achieve much more uniform ionomer distributions, with good coverage of the majority of catalyst particles [15].

4. Discussion

Changes in F 1s spectra, integrated amounts of ionomer, and 3D ionomer distributions caused by radiation damage during soft X-ray tomography measurements have been studied. The effects of total dose, sample thickness, number of projection angles, and choice of measurement energies have been explored. High incident flux and/or use of many projection angles, and thus large total dose (> 50 MGy) results in unacceptable levels of spectral (and thus chemical) change, mass loss, and modifications of the 3D spatial distributions. Reducing the incident flux and using a slight defocus (to 50 nm, the same as the pixel step size), results in tomographic data sets in which changes from radiation damage are barely measurable (code F, G). The advanced compressed sensing reconstruction method [41] allowed a significant decrease in the number of tilt angles needed. This greatly decreased the radiation dose, and also decreased the measurement time from ~12 h to ~4 h (of which $< 1/3$ rd is actual beam-on-sample time). CS reconstruction allows good quality reconstructions with astonishingly small numbers of sample tilt angles. Systematically predicting the ROI at each tilt angle and modifying the acquisition software to enable auto positioning and auto focus will allow further reduction of the acquisition time.

Supplemental section S-6 (including Fig. S-10) summarizes the quantitative radiation damage aspects of this study. These results indicate that STXM tomography at room temperature can be used to measure meaningful 3D distributions of ionomer in PEM-FC cathodes if sufficient care is used in making the measurements, and if advanced

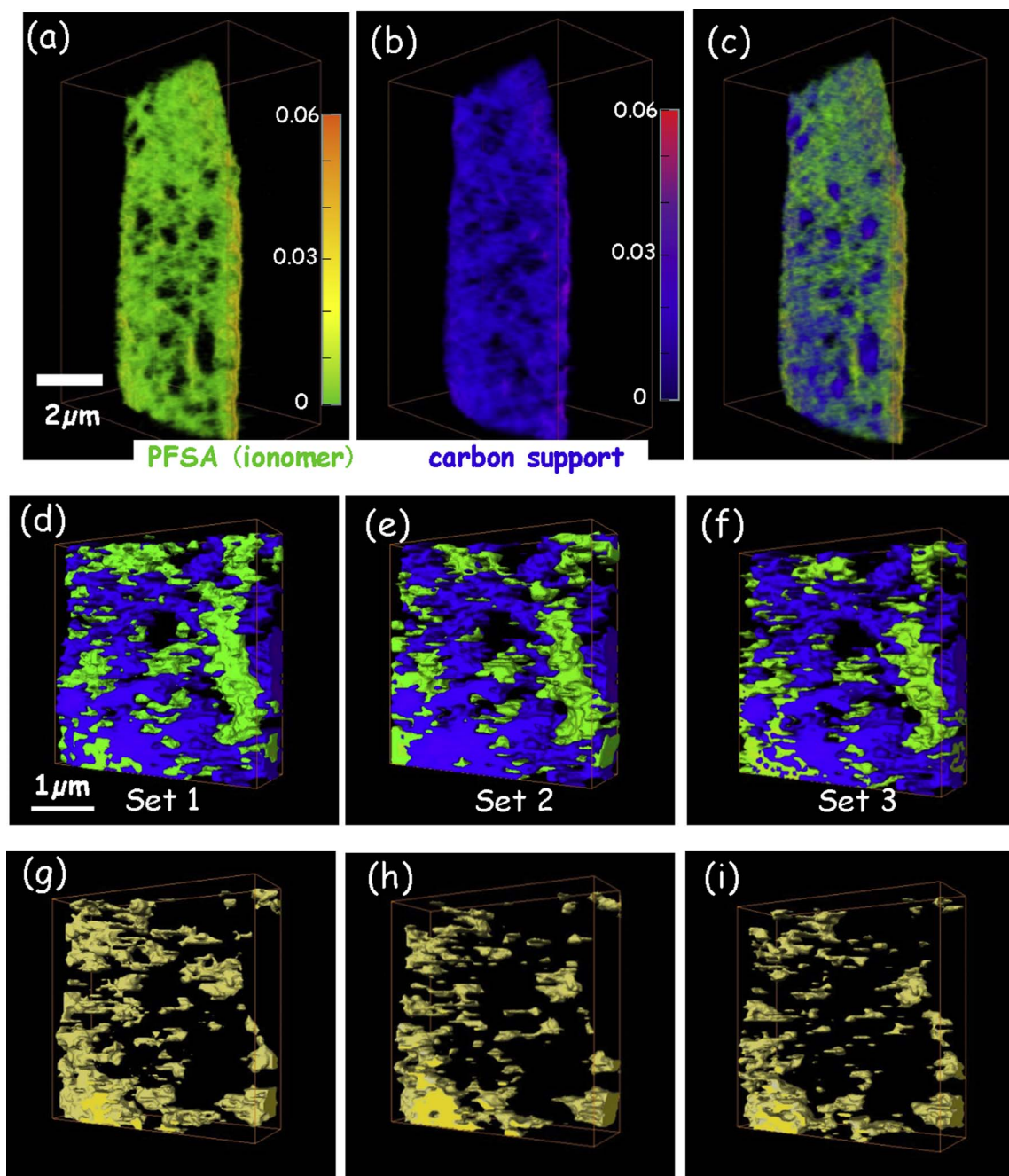


Fig. 7. 3D distributions of the cathode of sample MEA-A, tomography measurement code F (a) PFSA (green) from OD₇₀₅ – OD₆₈₄, (b) carbon support (blue) from OD_{284.5} – OD₂₈₀. The scale bars on the right side of (a), (b) indicate the voxel intensity scale, for a voxel size of (50 nm)³. (c) composite of the 2 components, in each case viewed at -45° . Threshold for ionomer is 0.007, that for carbon support is 0.005. Surface rendered 3D distributions of PFSA (green), carbon support (blue) in a region of the cathode of sample MEA-A, tomography measurement code F, viewed at a tilt of -30° . (d) set 1, (e) set 2, (f) set 3. (g), (h), (i) are surface renderings of the intersection of the maps of the carbon support and ionomer for sets 1, 2 and 3. Thresholds for the ionomer distributions are 0.007, 0.0033, 0.0036 (OD/voxel) for sets 1, 2 and 3, while those for the carbon support were 0.005 for each set. (measured at ALS 5.3.2.2).

reconstruction methods like compressed sensing [41] are used. A major challenge for STXM tomography applied to ionomer-in-cathode distributions is that only limited 3D information can be obtained because of the need to use thin sections on account of the strong absorption at the C 1s (and to a lesser extent) F 1s edges. The resolution in the z-direction is at best 50 nm. Thus only 2–6 unique samplings along the z-direction are being made in these measurements. Although the lateral spatial resolution in 2D projection images can be as small as 30 nm if a 25 nm outer zone diameter zone plate is used, the 3D spatial resolution is lower than that for 2D projection due to a number of factors including: misalignment of images measured at different tilt angles, the missing wedge effect, out-of-focus images at high rotation angles, etc. If

the alignment across tilt angles can be improved this may increase the 3D spatial resolution.

Supplemental section S-7 (including Supplemental Figs. S-10) discusses the 3D spatial resolution of these measurements, which is estimated to be ~ 90 nm, limited by the large pixel size (50 nm) and other factors. Another issue that affects the results is the threshold used for each dataset. The Otsu auto threshold method [61] was used to guide choice of threshold for segmentation in all cases, and in general the threshold chosen was very close to those values. However, the signal to noise level affects the threshold that approach generates. Masking and removing the non-cathode regions (membrane and embedding polymer) before reconstruction and using the same parameters for

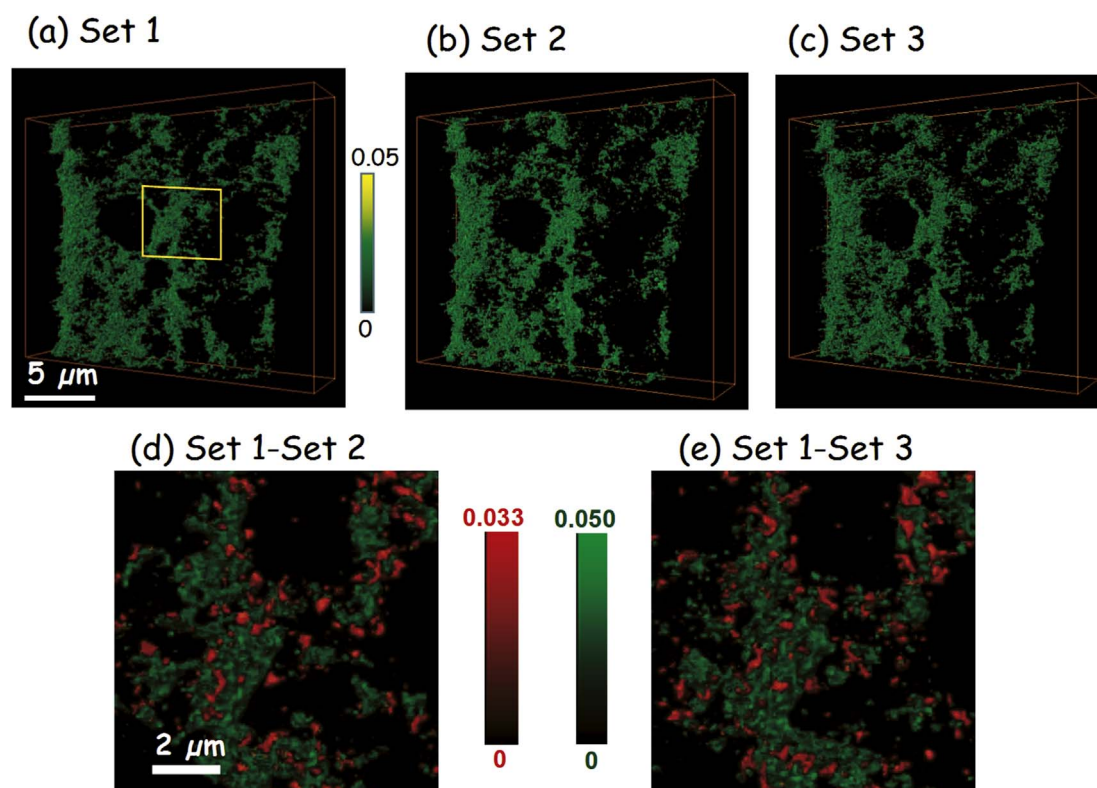


Fig. 8. 3D distributions of ionomer in cathode (green) from 3-set tomography sample MEA 11-GDE, tomography measurement code G, viewed at -30° . Total volume of cathode region of (a) set 1, (b) set 2, (c) set 3. (d) set 2 (green) and the difference between set 1 and set 2. (e) set 3 (green) and the difference between set 1 and set 3 in the yellow box region. In (d) and (e) red displays the ionomer signal present in the earlier measurement that is absent in the later measurement, while green is the signal present in both measurements. Thresholds for each data set are 0.0042, 0.0045 and 0.0046. (measured at CLS a-STXM, 10ID1).

reconstruction, rendering and thresholding will minimize this source of systematic uncertainty. We note that the data sets were measured using different beamlines which have different properties. We have tried as best we could to compensate by e.g. using beamline specific detector efficiencies, in some cases measured using the method reported in Ref. [63].

Supplemental section S7 (with Fig. S-11) provides a check on the accuracy of the 4D imaging by comparing projections of 3D data with 2D measurements.

This work shows that STXM tomography at room temperature can be used to quantify 3D distributions of ionomer in PEM-FC cathodes with negligible radiation damage. This is the first time the 3D distribution of the PFSA ionomer-in-cathode is shown in its original state without chemically staining to enhance contrast [17,18] or modified due to excess radiation damage [19], or by sample preparation technique [64]. We have also demonstrated that the damage caused to the PFSA ionomer due to soft X-rays is not homogenous in 3D. Therefore, a simple extrapolation of the 3D volume of the ionomer to compensate for the damage will not yield accurate information about the sample. Since X-rays and electrons cause similar structural changes to the ionomer due to damage [10], we believe this is of major concern for those performing electron tomography as a means to measure the 3D distributions of ionomer in PEM-FC electrodes.

5. Future developments

STXM tomography with compressed sensing reconstruction was used to measure 3D distributions of ionomer in the cathodes of PEMFC catalyst coated membranes. By systematically reducing total dose and using compressed sensing for 3D reconstruction, 3D ionomer distributions have been measured under conditions where changes from radiation damage are barely measurable. Measuring samples at low

temperature (100 K) can further improve reliability of determining ionomer distributions in 3D since the F-loss should be suppressed [65]. STXM cryo-tomography is now available at the CLS [66] and measurements are underway to verify this claim.

The emerging technique of soft X-ray ptychography [67] has been applied to 4D imaging of PEM-FC cathodes [20,68]. Ptychography has higher spatial resolution than STXM, having achieved better than 5 nm in 2D projection imaging [67]. However, ptycho-tomography uses much higher X-ray doses and thus the radiation damage issue is more severe than conventional ambient temperature STXM tomography. High spatial resolution (12 nm) 2D projection mapping of PFSA ionomer in cathodes of a PEM-FC has been achieved with low dose ptychography [20,68]. We expect that the COSMIC beamline and ptychography end stations presently being commissioned at the ALS will have the potential to perform 4D imaging of ionomer in PEM-FC electrodes with spectro-ptycho-tomography with acceptable doses and extent of radiation damage.

Acknowledgements

We thank Martin Obst (Bayreuth University) for making the tomography rotation stage used in this study. Research was funded by NSERC (RGPIN6141-15), AFCC (10592538), the CarPE-FC fuel cell network (APCPJ417858-11) and the Canada Research Chair program (CRC-22684). Measurements were made using STXMs on beamlines 5.3.2.2 and 11.0.2 at the Advanced Light Source which is supported by the Division of Basic Energy Sciences of U.S. DoE under contract No. DE-AC02-05CH11231. Measurements were also made using the ambient STXM on beamline 10ID1 at the Canadian Light Source, which is supported by CFI, NSERC, CIHR, NRC and the University of Saskatchewan.

Appendix A. Supplementary data

Supplementary data related to this article can be found at <http://dx.doi.org/10.1016/j.jpowsour.2018.01.074>.

References

- [1] Z. Weber, R.L. Borup, R.M. Darling, P.K. Das, T.J. Dursch, W. Gu, D. Harvey, A. Kusoglu, S. Litster, M.M. Mench, R. Mukundan, J.P. Owejan, J.G. Pharoah, M. Secanell, I.V. Zenyuk, *J. Electrochem. Soc.* 161 (2014) F1254–F1299.
- [2] R.F. Egerton, R.F., P. Li, M. Malac, *Micron* 35 (2004) 399–409.
- [3] R.F. Egerton, *Ultramicroscopy* 127 (2013) 100–108.
- [4] J. Wang, C. Morin, L. Li, A.P. Hitchcock, X. Zhang, T. Araki, A. Doran, A. Scholl, *J. Electron. Spectrosc. Relat. Phenom.* 170 (2009) 25–36.
- [5] S.P. Williams, C.J. Jacobsen, X. Kirz, J. Zhang, J. Van't Hof, S. Lamm, *Proc. SPIE - The International Society for Optical Engineering* 1741 (1993) 318–324.
- [6] D.T. Grubb, *J. Mater. Sci.* 9 (1974) 1715–1736.
- [7] T. Coffey, S.G. Urquhart, H. Ade, *J. Electron. Spectrosc. Relat. Phenom.* 122 (2002) 65–78.
- [8] S. Yakovlev, P.N. Balsara, H.K. Downing, *Membranes* 3 (2013) 424–439.
- [9] D.A. Cullen, R. Koestner, R.S. Kukreja, Z.Y. Liu, S. Minko, O. Trotsenko, A. Tokarev, L. Guetaz, H.M. Meyer, C.M. Parish, K.L. More, *J. Electrochem. Soc.* 161 (2014) F1111–F1117.
- [10] L.G.A. Melo, A.P. Hitchcock, J. Jankovic, J. Stumper, D. Susac, V. Berejnov, *ECS Transactions* 80 (2017) 275–282.
- [11] D. Susac, V. Berejnov, A.P. Hitchcock, J. Stumper, *ECS Transactions* 50 (2012) 405–413.
- [12] D. Susac, V. Berejnov, A.P. Hitchcock, J. Stumper, *ECS Transactions* 41 (2011) 629–635.
- [13] A.P. Hitchcock, V. Berejnov, V. Lee, M.M. West, M. Dutta, V. Colbow, S. Wessel, *J. Power Sources* 266 (2014) 66–78.
- [14] A.P. Hitchcock, V.J. Wu Lee, N. Appathurai, T. Tyliczszak, H.-W. Shiu, D. Shapiro, V. Berejnov, D. Susac, *J. Stumper, Microsc. Microanal.* 22 (S-3) (2016) 1290–1291.
- [15] A.P. Hitchcock, V. Lee, J. Wu, M.M. West, G. Cooper, V. Berejnov, T. Soboleva, D. Susac, *J. Stumper, Am. Inst. Phys. Conf Series* 1696 (2016) 020012 (1–8).
- [16] D. Putz, V. Susac, J. Berejnov, A.P. Wu, Hitchcock, J. Stumper, *J. Electrochem. Soc.* 75 (2016) 3–23.
- [17] H. Uchida, J.M. Song, S. Suzuki, E. Nakazawa, N. Baba, M. Watanabe, *J. Phys. Chem. B* 110 (2006) 13319–13321.
- [18] M. Lopez-Haro, L. Guétaz, T. Printemps, A. Morin, S. Escribano, P.H. Jouneau, P. Bayle-Guillemaud, F. Chandezon, G. Gebel, *Nat. Commun.* 5 (2014) 5229.
- [19] V. Berejnov, D. Susac, J. Stumper, A.P. Hitchcock, *ECS Transactions* 50 (2013) 361–368.
- [20] A.P. Hitchcock, *J. Electron. Spectrosc. Relat. Phenom.* 200 (2015) 49–63.
- [21] U. Bonse, A. Tkachuk, M. Feser, H. Cui, F. Diewer, H. Chang, W. Yun, *SPIE Proceedings* 6318 (2006) 63181D.
- [22] W.K. Epting, W.K., J. Gelb, S. Litster, *Adv. Funct. Mater.* 22 (2012) 555–560.
- [23] Z. Fishman, J. Hinebaugh, A. Bazylak, *J. Electrochem. Soc.* 157 (2010) B1643–B1650.
- [24] P. Krüger, H. Markötter, J. Hausmann, M. Klages, T. Arlt, J. Banhart, C. Hartnig, I. Manke, J. Scholta, *J. Power Sources* 196 (2011) 5250–5255.
- [25] J. Lee, J. Hinebaugh, A. Bazylak, *J. Power Sources* 227 (2013) 123–130.
- [26] F.H. Garzon, S.H. Lau, J.R. Davey, R. Borup, *ECS Transactions* 11 (2007) 1139–1149.
- [27] T. Saida, O. Sekizawa, N. Ishiguro, M. Hoshino, K. Uesugi, T. Uruga, S.-I. Ohkoshi, T. Yokoyama, M. Tada, *Angew. Chem. Int. Ed.* 51 (2012) 10311–10314.
- [28] H. Matsui, N. Ishiguro, T. Uruga, O. Sekizawa, K. Higashi, N. Maejima, M. Tada, *Angew. Chem. Int. Ed.* 56 (2017) 9371–9375.
- [29] W. Chao, B.D. Harteneck, J.A. Liddle, E.H. Anderson, D.T. Attwood, *Nature* 435 (2005) 1210–1213.
- [30] A. Sakidiniwat, D. Attwood, *Nat. Photon.* 4 (2010) 840–848.
- [31] G.A. Johansson, J.J. Dynes, A.P. Hitchcock, T. Tyliczszak, G.D.W. Swerhone, J.R. Lawrence, *Proc. SPIE* 6318 (2006) 11-1–9.
- [32] G.A. Johansson, J.J. Dynes, A.P. Hitchcock, T. Tyliczszak, G.D. Swerhone, J.R. Lawrence, *Microsc. Microanal.* 12 (2006) 1412–1413.
- [33] G.A. Johansson, T. Tyliczszak, G.E. Mitchell, M.H. Keefe, A.P. Hitchcock, *J. Synchrotron Radiat.* 14 (2007) 395–402.
- [34] A.P. Hitchcock, J.J. Dynes, G. Johansson, J. Wang, G. Botton, *Micron* 39 (2008) 311–319.
- [35] A.P. Hitchcock, G.A. Johansson, G.E. Mitchell, M.H. Keefe, T. Tyliczszak, *Appl. Phys. A* 92 (2008) 447–452.
- [36] G. Schmid, M. Obst, J. Wu, A.P. Hitchcock, C.S.S.R. Kumar (Ed.), Chapter 2 in *X-ray and Neutron Techniques for Nanomaterials Characterization*, vol. 5, Springer, Berlin, 2016, pp. 43–94 2016.
- [37] M. Howells, C. Jacobsen, T. Warwick, A. Van den Bos, P.W. Hawkes, J.C.H. Spence (Eds.), *Science of Microscopy*, Springer New York, New York, NY, 2007, pp. 835–926.
- [38] H. Ade, A.P. Hitchcock, *Polymer* 49 (2008) 643–675.
- [39] A.P. Hitchcock, Gustaaf Van Tendeloo, Dirk Van Dyck, Stephen J. Pennycook (Eds.), Chapter 22 in *Volume II of the Handbook on Nanoscopy*, Wiley, 2012, pp. 745–791.
- [40] M.G. George, J. Wang, R. Banerjee, A. Bazylak, *J. Power Sources* 309 (2016) 254–259.
- [41] J. Wu, M. Lerotic, S. Collins, R. Leary, Z. Saghi, P. Midgley, V. Berejnov, D. Susac, J. Stumper, G. Singh, A.P. Hitchcock, *Microsc. Microanal.* 23 (2017) 951–966.
- [42] R. Takekoh, M. Okubo, T. Araki, H.D.H. Stöver, A.P. Hitchcock, *Macromolecules* 38 (2005) 542–551.
- [43] K.V. Kaznatcheev, Ch Karunakaran, U.D. Lanke, S.G. Urquhart, M. Obst, A.P. Hitchcock, *Nucl. Inst. Meth. A* 582 (2007) 96–99.
- [44] T. Warwick, H. Ade, A.L.D. Kilcoyne, M. Kritscher, T. Tyliczszak, S. Fakra, A.P. Hitchcock, P. Hitchcock, H.A. Padmore, *J. Synchrotron Radiat.* 9 (2002) 254–257.
- [45] H. Bluhm, K. Andersson, T. Araki, K. Benzerara, G.E. Brown, J.J. Dynes, S. Ghosal, M.K. Gilles, H. Ch. Hansen, J.C. Hemminger, A.P. Hitchcock, G. Ketteler, A.L.D. Kilcoyne, E. Knedler, J.R. Lawrence, G.G. Leppard, J. Majzlam, B.S. Mun, S.C.B. Myneni, A. Nilsson, H. Ogasawara, D.F. Ogletree, K. Pecher, M. Salmeron, D.K. Shuh, B. Tonner, T. Tyliczszak, T. Warwick, T.H. Yoon, *J. Electron. Spectrosc. Relat. Phenom.* 150 (2006) 86–104.
- [46] A.L.D. Kilcoyne, T. Tyliczszak, W.F. Steele, S. Fakra, P. Hitchcock, K. Franck, E. Anderson, B. Harteneck, E.G. Rightor, G.E. Mitchell, A.P. Hitchcock, L. Yang, T. Warwick, H. Ade, *J. Synchrotron Radiat.* 10 (2003) 125–136.
- [47] J. Stöhr, *NEXAFS Spectroscopy*, Springer, Berlin, 1992.
- [48] D.A. Shapiro, R. Celestre, P. Denes, M. Farmand, J. Joseph, A.L.D. Kilcoyne, S. Marchesini, H. Padmore, S.V. Venkatakrisnan, T. Warwick, Y.-S. Yu, *J. Phys. Conf. Ser* 849 (2017) 012028.
- [49] D.L. Donoho, *IEEE Trans. Inf. Theor.* 52 (2006) 7–21.
- [50] Z. Saghi, G. Divitini, B. Winter, R. Leary, E. Spiecker, C. Ducati, P.A. Midgley, *Ultramicroscopy* 160 (2016) 230–238.
- [51] A.P. Hitchcock, aXis2000 is an IDL Program for Analysis of Spectromicroscopy Data. It is available free for non-commercial use from <http://unicorn.mcmaster.ca/aXis2000.html>.
- [52] C. Jacobsen, S. Wirick, G. Flynn, C. Zimba, *J. Microsc.* 197 (2000) 10–17.
- [53] J.R. Kremer, D.N. Mastrorade, J.R. McIntosh, *J. Struct. Biol.* 116 (1996) 71–76.
- [54] C. Messaoudi, T. Boudier, C.O.S. Sorzano, S. Marco, *BMC Bioinf.* 8 (2007) 288–312.
- [55] M. Lerotic, M.R. Mak, S. Wirick, F. Meirer, C. Jacobsen, *J. Synchrotron Radiat.* 21 (2014) 1206–1212.
- [56] MANTIS is a python code for spectromicroscopy data analysis, available free at <http://spectromicroscopy.com>.
- [57] T. Elfving, P. Hansen, T. Nikazad, *SIAM J. Sci. Comput.* 34 (2012) A2000–A2017.
- [58] E.Y. Sidky, X. Pan, *Phys. Med. Biol.* 53 (2008) 4777–4799.
- [59] E.F. Pettersen, T.D. Goddard, C.C. Huang, G.S. Couch, D.M. Greenblatt, E.C. Meng, T.E. Ferrin, *J. Comput. Chem.* 25 (2004) 1605–1612.
- [60] M. Westerhoff Stalling, H. Hege, H.-C.C.D. Hansen, C.R. Johnson (Eds.), "Amira: a Highly Interactive System for Visual Data Analysis". *The Visualization Handbook*, Elsevier, 2005, pp. 749–767.
- [61] N. Otsu, *Automatica* 11 (1975) 23–27.
- [62] L.G.A. Melo, M. West, V. Berejnov and A.P. Hitchcock, *Radiation Physics and Chemistry*, (in preparation).
- [63] A.F.G. Leontowich, A.P. Hitchcock, T. Tyliczszak, M. Weigand, J. Wang, C. Karunakaran, *J. Synchrotron Radiat.* 19 (2012) 976–987.
- [64] L.G.A. Melo, G.A. Botton, A.P. Hitchcock, *Microsc. Microanal.* 21 (2015) 2443–2444.
- [65] J. Wang, C.J. Jacobsen, J. Maser, J. Osanna, *J. Microsc.* 197 (2000) 80–93.
- [66] A.F.G. Leontowich, R.B., C. Regier, D.M. Taylor, J. Wang, D. Beauregard, J. Geilhufe, J. Swirsky, J. Wu, C. Karunakaran, A. P. Hitchcock, and S. G. Urquhart, *Revn. Sci Inst* (in prep).
- [67] D.A. Shapiro, Y.-S. Yu, T. Tyliczszak, J. Cabana, R. Celestre, W. Chao, K. A.L.D. Kaznatcheev, F. Kilcoyne, S. Maia, Y.S. Marchesini, T. Meng, L.L. Warwick, Yang, H.A. Padmore, *Nat. Photonics* 8 (2014) 765–769.
- [68] J. Wu, X. Zhu, T. Tyliczszak, H.-W. Shiu, D. Shapiro, V. Berejnov, D. Susac, J. Stumper and A. P. Hitchcock, *J. Synchrotron Radiat.* (in prep).